PHOTONICS Research

Dynamic bifunctional THz metasurface via dual-mode decoupling

Xuan Cong,[1] (ID) Hongxin Zeng,[1] Shiqi Wang,[1] Qiwu Shi,[2] Shixiong Liang,[3] Jiandong Sun,[4] Sen Gong,[1,2] (ID) Feng Lan,[1,5] Ziqiang Yang,[1,5] (ID) and Yaxin Zhang[1,5,*]

[1]Terahertz Science and Technology Research Center, University of Electronic Science and Technology of China, Chengdu 610000, China
[2]College of Materials Science and Engineering, Sichuan University, Chengdu 610065, China
[3]National Key Laboratory of Application Specific Integrated Circuit, Hebei Semiconductor Research Institute, Shijiazhuang 050051, China
[4]Key Laboratory of Nanodevices and Applications, Suzhou Institute of Nano-Tech and Nano-Bionics (SINANO), Chinese Academy of Sciences, Suzhou 215123, China
[5]Yangtze Delta Region Institute (HuZhou), University of Electronic Science and Technology of China, Huzhou 313001, China
*Corresponding author: zhangyaxin@uestc.edu.cn

Metasurfaces have powerful light field manipulation capabilities and have been researched and developed extensively in various fields. With an increasing demand for diverse functionalities, terahertz (THz) metasurfaces are also expanding their domain. In particular, integrating different functionalities into a single device is a compelling domain in metasurfaces. In this work, we demonstrate a functionally decoupled THz metasurface that can incorporate any two functions into one metasurface and switch dynamically through external excitation. This proposed metasurface is formed by the combination of split-ring resonators and phase change material vanadium dioxide (VO$_2$). It operates in the single-ring resonant mode and double-ring resonant mode with varying VO$_2$ in insulating and metallic states, respectively. More importantly, the phase modulation is independent in two operating modes, and both cover a 360° cross-polarized phase with efficient polarization conversion. This characteristic makes it obtain arbitrary independent phase information on the metasurface with different modes to switch dual functions dynamically. Here, we experimentally demonstrate the functions of a tunable focal length and large-angle focus deflection of a THz off-axis parabolic mirror to verify the dual-function switching characteristics of the functionally decoupled metasurface. The functionally decoupled metasurface developed in this work broadens the way for the research and application of multifunctional modulation devices in the THz band. © 2022 Chinese Laser Press

https://doi.org/10.1364/PRJ.453496

1. INTRODUCTION

Metamaterials can flexibly control the amplitude, phase, and polarization of light at the sub-wavelength scale. Their appearance has mostly changed the way in which we manipulate electromagnetic waves, thus breaking through many limitations of traditional optics. Due to their unique and novel properties, metamaterials play an important role in various fields and realize a variety of functions, such as holographic imaging [1–3], beam deflectors [4–6], perfect absorbers [7–10], and flat lenses [11–15]. With the expansion of application fields, higher requirements are put forward for metamaterials, especially for functionally decoupling metamaterials that can integrate different functions into a single device. At present, the common method of decoupling functions of metamaterials is spin decoupling with circular polarization incidence [16–21], which realizes polarization-related components by simultaneously

controlling the phase of orthogonally polarized waves, thereby realizing different functions. However, this method cannot realize flexibly dynamic function switching because it needs to switch the polarization state of the electromagnetic signal to realize different functions. It is evident that a dynamic metamaterial with response to external excitation signals is a potential approach.

At microwave frequencies, electronically controlled metasurfaces [22–26] with integrated diodes have become a very attractive control method due to their tuning flexibility. However, when this method is extended to higher frequencies, there is a lack of corresponding functional electronic devices, and it is quite difficult to integrate electrodes into each structure. Therefore, in the terahertz (THz) band, many researchers are committed to realizing actively tunable metamaterials by introducing materials with external field induction response, such as two-dimensional material graphene [27–30], liquid

crystal [31–34], and phase change materials [3,35]. Especially, vanadium dioxide (VO$_2$) has attracted much attention because of its phase transition temperature close to room temperature. In the past few years, a great deal of attention has been paid to the study of VO$_2$ multilayer structure [36,37], nanostructure [38–40], and opal and photonic bandgap structure [41], which has greatly promoted the combination of VO$_2$ and metamaterials [42–44]. However, the above-mentioned THz tunable metamaterials are based on the principle of phase compensation and cannot achieve complete phase reconstruction. The phase change of one state often affects another state, thus different functions are usually related to each other, and complete functional decoupling cannot be realized.

In this paper, we experimentally demonstrate a dynamic bifunctional metamaterial embedded with VO$_2$ that has strong mode independence and can achieve overall phase reconstruction instead of phase compensation. It integrates the functions of polarization conversion and phase modulation, and has modulation effects for multiple polarizations. By changing the temperature of the active area, the phase transformation characteristics of VO$_2$ can be excited, and the operation mode of the superatom can be changed; thus one can dynamically tune the working state and function of the metasurface. Through the combination of the transmission phase and Pancharatnam-Berry (P-B) phase, both modes can achieve 360° phase coverage, and we use a reflective structure that has the advantages of low loss and easy manufacturing and also has high efficiency and good performance. More importantly, the modulation effects of these two operation modes [single-ring resonant mode (S-mode) and double-ring resonant mode (D-mode)] are independent of each other, which means we can design completely different functions for the two operation modes and ensure the efficiency of both.

As a verification, we experimentally demonstrate a thermally-controlled tunable THz off-axis parabolic mirror embedded with VO$_2$, as shown in Fig. 1, which can not only tune the focal length but also achieve a large-angle deflection of the focus, providing a new method for the design of multifunctional modulation devices in the THz band. As an extension, other phase change materials and different control methods, such as light control and electric control, can also be used to fulfill this and other related functions.

2. DESIGN AND THEORY

As a phase change material, the resistivity of VO$_2$ changes up to four orders of magnitude before and after the phase change, and its phase change rate is only tens of femtoseconds. VO$_2$ is approximately in an insulating state (I-VO$_2$) at 300 K, and its dielectric constant $\varepsilon = 9$, with the conductivity of 30 S/m. When the temperature exceeds the phase change temperature of 341 K, VO$_2$ will undergo a transition from an insulating state to a metallic state (M-VO$_2$). The complex permittivity in the THz band can be described by the Drude model [45–47]:

$$\varepsilon(\omega) = \varepsilon_\infty - \frac{\omega_n^2(\sigma_0)}{\omega^2 + i\gamma\omega}, \tag{1}$$

where the first term is the high-frequency limit constant, $\varepsilon_\infty = 12$, $\gamma = e/km^*$ represents the collision frequency, m^*
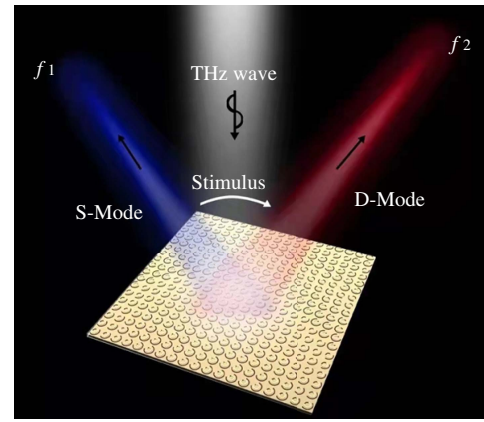

Fig. 1. Schematic diagram of dynamic function switching of THz waves via mode decoupling controlled by external physical field stimulus. When y- (or x-) polarized waves impinge vertically, the reflected waves undergo polarization conversion and produce independent phase shifts in the two modes, achieving different functions.

is the effective optical mass of the electron, and $\omega_n(\sigma)$ indicates that the conductivity is related to the plasma frequency, because σ is proportional to the free carrier density. According to Refs. [45,46], it can be taken as $\sigma_0 = 3 \times 10^5$ S/m, $\omega_n(\sigma_0) = 1.4 \times 10^{15}$ rad/s, $\gamma = 5.75 \times 10^{13}$ rad/s.

For the design in this paper, the composite superatom structure of metal combined with VO$_2$ is shown in Fig. 2(a). The substrate is quartz with a dielectric constant of 3.75, the back is a continuous gold film, and the front is a concentric ring tilted 45° relative to the x axis. The inner ring is complementary gold-split resonant ring (G-SRR) and VO$_2$-SRR (V-SRR), and the outer ring is V-SRR with a larger radius. We used the electromagnetic simulation software CST to simulate the unit structure, where x and y directions use the unit cell boundary, the z direction uses the open add space boundary, the y-polarized wave is irradiated vertically from the z direction, and the frequency domain solver is used to solve it. After parameter optimization, we determine that the cell period is $T = 270$ μm, thickness of the quartz substrate is $D = 100$ μm, radius of the inner ring is $r = 67$ μm, radius of the outer ring is
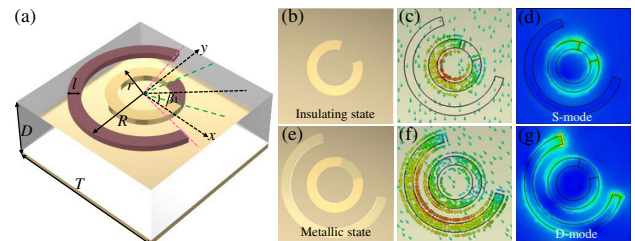

Fig. 2. (a) Schematic diagram of the unit structure and parameter annotation. (b) Equivalent structure diagram, (c) surface current distribution, and (d) corresponding S-mode field distribution of the unit in the insulating state at normal temperature. (e) Equivalent structure diagram, (f) surface current distribution, and (g) corresponding D-mode field distribution of the unit in the metallic state at high temperature.

$R = 115$ μm, linewidth of all rings is $L = 20$ μm, and thickness of gold and VO_2 is $d = 300$ nm.

Due to the near-field interaction between the metal layers, the superatom supports the typical gap–surface plasmon resonance, forming a gap–surface plasmon metasurface and realizing orthogonal polarization transformation. In this way, each superatom can simultaneously and independently manipulate the polarization and phase of the reflected field at a thickness of sub-wavelength scale. At room temperature of 300 K, as shown in Fig. 2(b), VO_2 is in the insulating state, acting as a medium in the THz band, with low conductivity and high transmittance. It can be seen from Figs. 2(c) and 2(d) that the electric field is concentrated at both ends of the G-SRR due to inductance capacitance (LC) resonance. At this time, VO_2 hardly works; only the internal G-SRR works independently with single-ring resonance, modulating the polarization and phase of the reflected field, which we call S-mode. When the temperature of the active area rises to 341 K, as shown in Fig. 2(e), due to the phase change characteristics of VO_2 being excited, its conductivity increases, the transmittance is greatly reduced, and it transitions from the insulating state to the metallic state. It can be seen from Figs. 2(f) and 2(g) that the electric field is distributed in both the inner composite SRR and the outer V-SRR. At the moment, the field is affected by the closed inner ring and the outer V-SRR with double-ring resonance, which we call the D-mode.

Here, by introducing the Jones matrix [48], the relationship between reflected wave and incident wave can be expressed as follows [30,49]:

$$\begin{pmatrix} R_x \\ R_y \end{pmatrix} = \begin{pmatrix} r_{xx} & r_{xy} \\ r_{yx} & r_{yy} \end{pmatrix} \begin{pmatrix} I_x \\ I_y \end{pmatrix}, \qquad (2)$$

where I_x, I_y, R_x, and R_y are the complex amplitudes of the incident and reflected wave components in x and y directions, respectively. Here, r_{mn} denotes that the incident n-polarized light converts to reflected m-polarized light. The polarization conversion ratio (PCR) for linearly polarized light can be written as follows [44,50]:

$$\text{PCR}(y) = \frac{|r_{xy}|^2}{|r_{xy}|^2 + |r_{yy}|^2} = \frac{R_{xy}}{R_{xy} + R_{yy}}. \qquad (3)$$

More importantly, we separately scanned the phase delay and reflectivity of the cross-polarized wave in the I-VO_2 and M-VO_2 states as a function of α_1 and α_2, where α_1 and α_2 are the opening angles of the inner gold ring and outer VO_2 ring, respectively, that is, the angles between the pink dotted lines and green dotted lines in Fig. 2(a). It can be seen from Figs. 3(a) and 3(b) that when VO_2 is in the insulating state, the cross-polarized wave reflectivity and phase change are almost related only to α_1, and α_2 has nearly no effect on it. Only the internal G-SRR works independently, that is, the S-mode is affected only by α_1. Conversely, when VO_2 is transformed into a metallic phase, it can be seen from Figs. 3(c) and 3(d) that the cross-polarized wave reflectivity and phase change are almost related only to α_2, and the inner complementary SRR is approximately a closed metal ring, resulting in α_1 having almost no effect on it. Therefore, the outer V-SRR and inner closed rings play a modulation role together, that is,
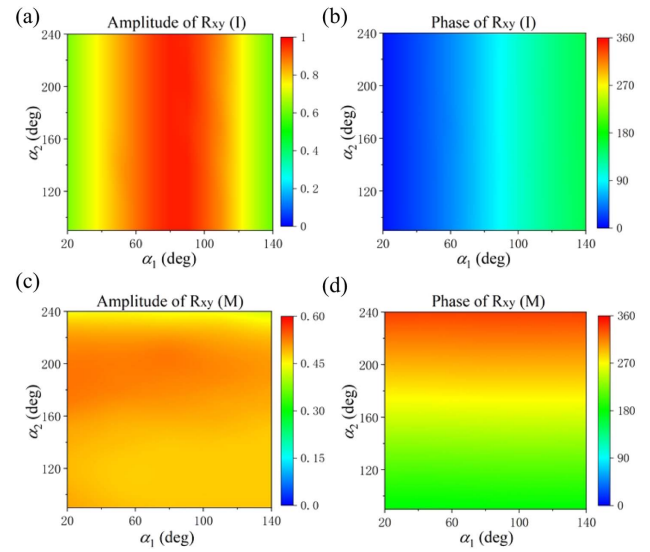

Fig. 3. (a) Amplitude of reflected cross-polarization wave in S-mode at room temperature and (b) corresponding phase delay. (c) Amplitude of reflected cross-polarization wave in high-temperature D-mode and (d) corresponding phase delay.

the D-mode is affected only by α_2. It can be seen that the two modes are independent and do not affect each other, which greatly increases the degree of freedom of dynamic control of metamaterials based on phase change materials, and further increases the possibility of related functional design.

Since the amplitudes of the last four elements are equal to the first four and the phase difference in the working frequency band is 180°, their reflection spectrum curves are no longer listed separately, and only their amplitude and phase characteristics are given at the 340 GHz frequency point. It can be seen from Figs. 4(a) and 4(b) that the cross-polarization phases of the selected units in both modes are linearly distributed with a higher amplitude, and the gradient is uniform in the working band. Further, we extracted the amplitude and phase characteristics of the selected unit at the atmospheric window frequency point of 340 GHz. As shown in Figs. 4(c) and 4(d), the cross-polarized wave amplitude in the S-mode is higher with certain fluctuations, while in the D-mode, the amplitude of the cross-polarized wave is relatively low, but the fluctuations are gentle and the consistency is better. The selected units in both modes have a phase gradient of 45° and can achieve 360° phase coverage under polarization conversion. According to the theory of coding metamaterials [51], we correspond to the phase "0°, 45°, 90°, 135°, 180°, 225°, 270°, 315°" of the selected cells in the two modes with "000, 001, 010, 011, 100, 101, 110, 111," respectively, so that the independent 3-bit coding design can be carried out in the two modes.

3. RESULTS AND DISCUSSION

To test the performance of the tunable THz metasurface we propose, we designed a zoomable off-axis parabolic mirror function for verification. According to the following Eq. (4) [52], we can calculate the phase distribution required for different focal positions:
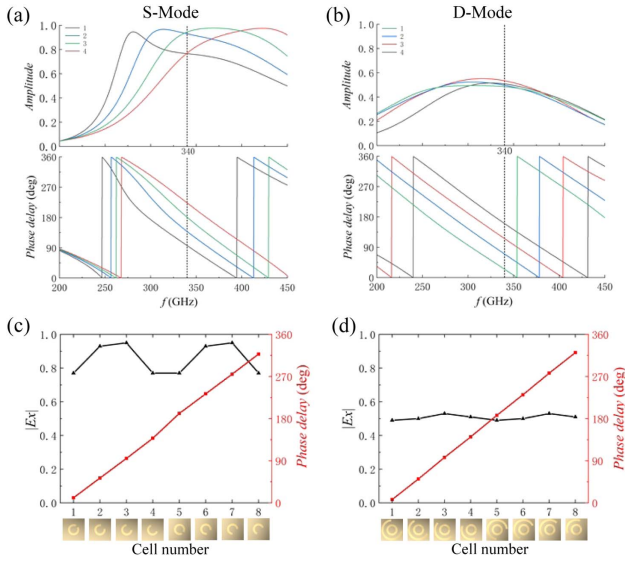
Fig. 4. (a) Spectra of the reflected cross-polarized wave (top) and corresponding phase delay (bottom) for forward illuminated *y*-polarized light in S-mode. (b) Spectra of the reflected cross-polarized wave (top) and corresponding phase delay (bottom) for forward illuminated *y*-polarized light in D-mode. Amplitude–phase distribution of reflected cross-polarization at 340 GHz for the selected superatom in (c) S-mode and (d) D-mode.

$$\varphi(x,y) = \frac{2\pi}{\lambda} \cdot n \cdot \left(\sqrt{f^2 + x^2 + y^2} - f \right), \qquad (4)$$

where λ is the working wavelength, f is the focal length, and n is the refractive index. Here, the medium is air, so $n = 1$, and (x, y) represents the coordinates of the superatoms in the parabolic mirror. The off-axis angle of the parabolic mirror we designed is 30°, and the focal length is 15 mm or 10 mm.

According to the corresponding phase encoding distribution, we arrange the superatom array and simulate the working state of the array in both modes. At room temperature of 300 K, VO_2 has high light transmittance, and only the inner metal ring of the superatom works; at this point, its working state is in S-mode. As shown in Fig. 5(a), when a *y*-polarized plane wave is vertically incident on the metasurface, the reflected wave becomes a cross-polarized wave and acquires appropriate phase shifts due to anisotropy, eventually focusing the reflected field 30° off-axis at a focal length of around $L = 15$ mm. According to Jones matrix theory and Eq. (4), the theoretical polarization conversion efficiency is calculated to be 77%. However, there is a part of the energy loss in the reflection process that cannot be ignored. When it is taken into account, the reflection efficiency is calculated to be 92.5%, so the effective conversion efficiency of the cross-polarized wave is 71.2%. As shown in Figs. 5(c)–5(e), we measured the intensity of the *x*-polarized wave with a THz camera at sections A ($L = 15$ mm), B ($L = 17$ mm), and C ($L = 20$ mm) corresponding to Fig. 5(a) along the normal direction of the focal plane. With the propagation distance increasing, the intensity of the focal spot gradually weakens, but the focal spot does not diverge, which is consistent with the result of the long focal depth displayed by the simulation. According to the result of the experiment, the effective conversion efficiency of
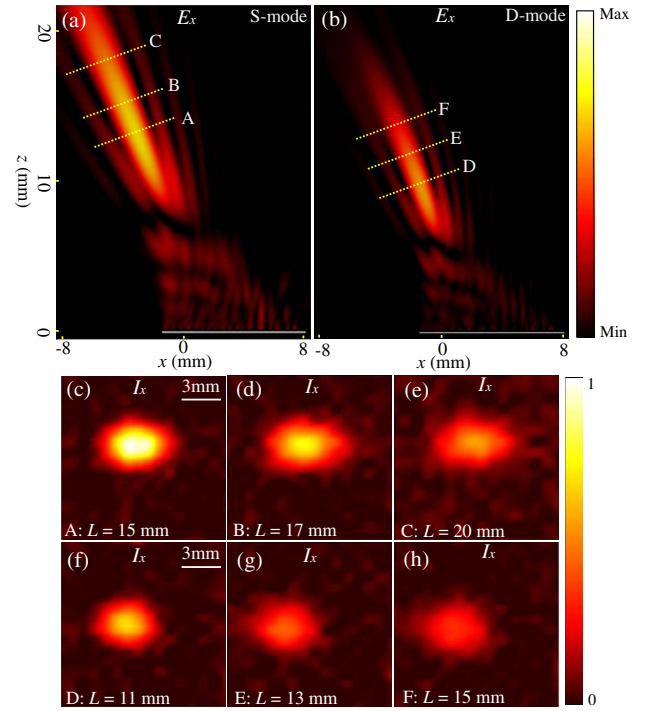

Fig. 5. Simulation and experimental results of the reflected cross-polarized wave focusing off-axis with tunable focal length when *y*-polarized wave is vertically incident. (a) Simulation results of E_x distribution in *xoz* plane in S-mode. (b) Simulation results of E_x distribution in *xoz* plane in D-mode. (c)–(e) Experimental results of I_x distribution measured at sections A ($L = 15$ mm), B ($L = 17$ mm), and C ($L = 20$ mm) in (a). (f)–(h) Experimental results of I_x distribution measured at sections D ($L = 11$ mm), E ($L = 13$ mm), and F ($L = 15$ mm) in (b).

the cross-polarized waves at $L = 15$ mm is 64.6%, and the focusing efficiency is 33.7%.

When the temperature of the active area increases above 341 K, the conductivity of VO_2 increases sharply, showing a metallic phase, and the light transmittance is greatly reduced. The inner complementary SRR is equivalent to a closed metal ring, which is coupled with the outer ring, and the superatom changes from the S-mode switch to the D-mode. At this moment, the anisotropy of the unit is reflected by the external V-SRR, and the working state of the designed metasurface also changes accordingly. As shown in Fig. 5(b), when the *y*-polarized plane wave is incident perpendicular to the metasurface, the focal direction of the reflected *x*-polarized wave is still 30° off-axis, but its focal length is significantly shortened, and the focal plane moves to around $L = 11$ mm. At this point, the theoretical polarization conversion efficiency calculated according to Eq. (3) is 72%, and the reflection efficiency is calculated as 39%; therefore, the effective conversion efficiency of the cross-polarized wave is 28%. It can be seen that the loss of the D-mode is much greater than that of the S-mode, which leads to a much smaller effective conversion efficiency of the cross-polarized wave of the D-mode. Similarly, we measured the *x*-polarization intensity distribution at sections D ($L = 11$ mm), E ($L = 13$ mm) and F ($L = 15$ mm) corresponding to Fig. 5(b) along the normal direction of the focal

plane. with a THz camera. As shown in Figs. 5(f)–5(h), with the increase in distance, the light spot gradually weakens. The measured effective conversion efficiency of the cross-polarized waves at the focal plane $L = 11$ mm is 23.2%, and the focusing efficiency is 11%.

Since the structure we propose is completely independent in the two modes, it can achieve not only phase compensation but also phase reconstruction, ensuring the functional decoupling of THz wave modulation in the two modes. Thereby, the metasurface can change not only the focal length but also the focus direction at a large angle by changing the coding combination of the two modes. At room temperature of 300 K, VO_2 is in the insulating state, and the superatom is in an S-mode. As shown in Fig. 6(a), the metamaterial we designed can convert the vertically incident y-polarized wave into an x-polarized wave, and focus it at the off-axis $+30°$ position, with a focal length near $L = 11$ mm. According to Eq. (3), it can be obtained that the theoretical polarization conversion efficiency is 75%, and the corresponding reflection efficiency is calculated to be 91%; hence, the effective conversion efficiency of the cross-polarized wave is 68.3%. Similarly, as shown in Figs. 6(c)–6(e), we measure the field distribution of the x-polarized waves at sections A ($L = 11$ mm), B ($L = 13$ mm), and C ($L = 15$ mm) corresponding to Fig. 6(a) along the normal direction of the focal plane. According to the experimental results, the effective conversion efficiency at

$L = 11$ mm is measured to be 63.3%, and the corresponding focusing efficiency is 32.4%.

When the designed metasurface is physically heated, VO_2 transitions from the insulating state to the metallic state, and the external V-SRR is coupled with the internal approximately closed loop. At this time, the superatom switches from the S-mode to the D-mode, and the modulation effect of the metasurface on the THz wave also changes accordingly. As shown in Fig. 6(b), when the y-polarized wave is vertically incident to the metasurface, the focal length of the reflected x-polarized wave is still 11 mm, but the focusing direction changes greatly, switching from $+30°$ on the right side of the axis to $–30°$ on the left side of the axis, achieving a focal deflection of about 60°. In the same way, we can obtain the effective conversion efficiency of the cross-polarized wave of 26.3%, with theoretical polarization conversion efficiency and reflection efficiency of 71% and 37%, respectively. As shown in Figs. 6(f)–6(h), the experimental results measured by the THz camera are consistent with the simulation basically. Its distribution characteristics are very similar to the corresponding field distribution of the S-mode, but the efficiency is relatively low, and the spot intensity is weak. The measured effective conversion efficiency at $L = 11$ mm is 21.4%, and the focusing efficiency is 12.1%.

By comparison, we find that the effective conversion efficiency of the cross-polarized wave of the experimental results is lower than that of the simulation results. This is likely due to the conductivity and permittivity of VO_2 depending greatly on the deposition techniques, and the conductivities of the two modes do not reach the preset value, which may cause the difference between the experiment and the simulation.

4. EXPERIMENT

The processing of the VO_2 composite THz metasurface begins with the preparation of VO_2 thin film. In this paper, we use the sol-gel method to prepare VO_2 films. The patterning of the VO_2 film uses inductive D-plasma etching (ICPE). First, we spin-coat the photoresist on the surface of the VO_2 film, and determine the pattern area of the VO_2 through photolithography and development. Then we use N_2 to etch the VO_2 film. Finally, through the process of photolithography-electron beam evaporation-stripping, 300 nm thick gold is vapor-deposited on the quartz substrate to form a metal artificial microstructure. The final processed product is shown in Figs. 7(a) and 7(b).

The measuring device is shown in Fig. 7(c). The 0.34 THz y-polarized THz wave emitted by a THz source is collimated by parabolic mirror 1 with a focal length of 177 mm and irradiated on parabolic mirror 2 with a focal length of 127 mm, and then the THz wave is reflected on the test sample by the mirror we prepared. Finally, the THz camera is used to collect the field distribution of the orthogonally polarized (x-polarized) THz wave on a predetermined plane in real time. The camera can work in the entire THz frequency range (0.1–10 THz) with an active area of 1.28 cm × 1.28 cm, composed of 32 × 32 pixels and a pixel interval of 0.4 mm. By integrating the data obtained from the camera, the THz power can be
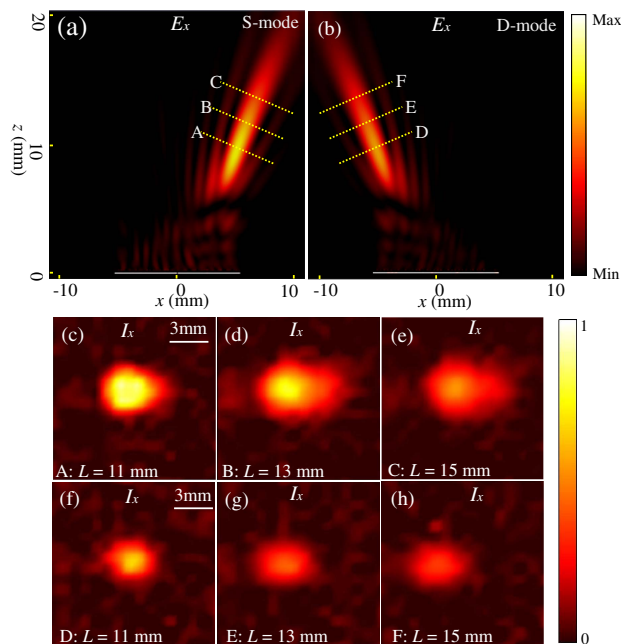
Fig. 6. Simulation and experimental results of the reflected cross-polarized wave focusing off-axis with large-angle focus deflection when y-polarized wave is vertically incident. (a) Simulation results of E_x distribution in xoz plane in S-mode. (b) Simulation results of E_x distribution in xoz plane in D-mode. (c)–(e) Experimental results of I_x distribution measured at sections A ($L = 11$ mm), B ($L = 13$ mm), and C ($L = 15$ mm) in (a). (f)–(h) Experimental results of I_x distribution measured at sections D ($L = 11$ mm), E ($L = 13$ mm), and F ($L = 15$ mm) in (b).
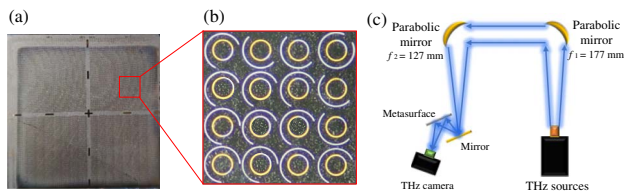
Fig. 7.   (a) Image of a fabricated metasurface sample and (b) its partially enlarged view. (c) Schematic diagram of the experimental setup.

calculated. After the metasurface sample is removed from the experimental device, it is replaced by another reflector. The total power can be calculated from the measured intensity distribution of the THz wave in the focal plane. The efficiency under different modulation functions is the ratio of the THz wave power collected under different conditions to the total power. It should be pointed out that because the test space near the sample is narrow in the test, the THz wave is not irradiated perpendicularly to the test sample, but has an incidence angle of about 10°. Hence, the actual receiving position of the camera is not 30° off-axis, but 40° off-axis. In addition, since the THz wave that is finally irradiated on the test sample in the optical path is not a strict plane wave but a spherical wave with a certain divergence angle, the actual measured focal spot size is larger than the preset. Furthermore, we found that there is THz transmission hysteresis in the devices during the experiment, which should be caused by the thermal hysteresis characteristic of VO_2 [40,53].

5. CONCLUSION

In this paper, we propose a dynamic bifunctional metasurface that combines patterned nano-scale VO_2 with metal microstructures. This metasurface can take advantage of the phase transition characteristics of VO_2 and present two modulation modes at room temperature and high temperature. Due to the independence of the two modes, not only off-axis focusing and zoom can be realized but also the large-angle deflection of off-axis focusing can be realized in the THz band. Furthermore, since each unit structure is symmetric with respect to the $x = y$ cross section, the design has a modulation effect on x-polarization, y-polarization, and circular polarization waves. More importantly, the off-axis parabolic mirror is used as an example to verify the performance of the designed metasurface, but the functions that the metasurface can achieve are more than these. Due to the independence of the two modes, we can achieve a combination of any two functions. In particular, through the combination with convolution theory, the diversity of its function modulation can be further enriched.

REFERENCES

1. D. Wen, F. Yue, G. Li, G. Zheng, K. Chan, S. Chen, M. Chen, K. F. Li, P. W. H. Wong, K. W. Cheah, E. Y. B. Pun, S. Zhang, and X. Chen, "Helicity multiplexed broadband metasurface holograms," Nat. Commun. **6**, 8241 (2015).
2. L. Jin, Z. Dong, S. Mei, Y. F. Yu, Z. Wei, Z. Pan, S. D. Rezaei, X. Li, A. I. Kuznetsov, Y. S. Kivshar, J. K. W. Yang, and C.-W. Qiu, "Noninterleaved metasurface for (2^6–1) spin- and wavelength-encoded holograms," Nano Lett. **18**, 8016–8024 (2018).
3. X. Liu, Q. Wang, X. Zhang, H. Li, Q. Xu, Y. Xu, X. Chen, S. Li, M. Liu, Z. Tian, C. Zhang, C. Zou, J. Han, and W. Zhang, "Thermally dependent dynamic meta-holography using a vanadium dioxide integrated metasurface," Adv. Opt. Mater. **7**, 1900175 (2019).
4. Y. Yuan, K. Zhang, X. Ding, B. Ratni, S. N. Burokur, and Q. Wu, "Complementary transmissive ultra-thin meta-deflectors for broadband polarization-independent refractions in the microwave region," Photon. Res. **7**, 80–88 (2019).
5. X. Yin, H. Zhu, H. Guo, M. Deng, T. Xu, Z. Gong, X. Li, Z. H. Hang, C. Wu, H. Li, S. Chen, L. Zhou, and L. Chen, "Hyperbolic metamaterial devices for wavefront manipulation," Laser Photon. Rev. **13**, 1800081 (2019).
6. L. Zhang, J. Ding, H. Zheng, S. An, H. Lin, B. Zheng, Q. Du, G. Yin, J. Michon, Y. Zhang, Z. Fang, M. Y. Shalaginov, L. Deng, T. Gu, H. Zhang, and J. Hu, "Ultra-thin high-efficiency mid-infrared transmissive Huygens meta-optics," Nat. Commun. **9**, 1481 (2018).
7. W. Wang, L. V. Besteiro, T. Liu, C. Wu, J. Sun, P. Yu, L. Chang, Z. Wang, and A. O. Govorov, "Generation of hot electrons with chiral metamaterial perfect absorbers: giant optical chirality for polarization-sensitive photochemistry," ACS Photon. **6**, 3241–3252 (2019).
8. A. Ghobadi, H. Hajian, B. Butun, and E. Ozbay, "Strong light–matter interaction in lithography-free planar metamaterial perfect absorbers," ACS Photon. **5**, 4203–4221 (2018).
9. B. Tang, Z. Li, E. Palacios, Z. Liu, S. Butun, and K. Aydin, "Chiral-selective plasmonic metasurface absorbers operating at visible frequencies," IEEE Photon. Technol. Lett. **29**, 295–298 (2017).
10. Y. Ren, T. Zhou, C. Jiang, and B. Tang, "Thermally switching between perfect absorber and asymmetric transmission in vanadium dioxide-assisted metamaterials," Opt. Express **29**, 7666–7679 (2021).
11. Q. Wang, X. Zhang, Y. Xu, Z. Tian, J. Gu, W. Yue, S. Zhang, J. Han, and W. Zhang, "A broadband metasurface-based terahertz flat-lens array," Adv. Opt. Mater. **3**, 779–785 (2015).
12. Z. Wang, T. Yang, Y. Zhang, Q. Ou, H. Lin, Q. Zhang, H. Chen, H. Y. Hoh, B. Jia, and Q. Bao, "Flat lenses based on 2D perovskite nanosheets," Adv. Mater. **32**, 2001388 (2020).
13. X.-T. Kong, A. A. Khan, P. R. Kidambi, S. Deng, A. K. Yetisen, B. Dlubak, P. Hiralal, Y. Montelongo, J. Bowen, S. Xavier, K. Jiang, G. A. J. Amaratunga, S. Hofmann, T. D. Wilkinson, Q. Dai, and H. Butt, "Graphene-based ultrathin flat lenses," ACS Photon. **2**, 200–207 (2015).
14. F. Ding, Y. Chen, and S. I. Bozhevolnyi, "Gap-surface plasmon metasurfaces for linear-polarization conversion, focusing, and beam splitting," Photon. Res. **8**, 707–714 (2020).
15. W. Ma, D. Jia, X. Yu, Y. Feng, and Y. Zhao, "Reflective gradient metasurfaces for polarization-independent light focusing at normal or oblique incidence," Appl. Phys. Lett. **108**, 071111 (2016).
16. C. Zheng, J. Li, G. Wang, J. Li, S. Wang, M. Li, H. Zhao, Z. Yue, Y. Zhang, Y. Zhang, and J. Yao, "All-dielectric chiral coding metasurface

based on spin-decoupling in terahertz band," Nanophotonics **10**, 1347–1355 (2021).

17. A. Arbabi, Y. Horie, M. Bagheri, and A. Faraon, "Dielectric metasurfaces for complete control of phase and polarization with subwavelength spatial resolution and high transmission," Nat. Nanotechnol. **10**, 937–943 (2015).

18. J. P. Balthasar Mueller, N. A. Rubin, R. C. Devlin, B. Groever, and F. Capasso, "Metasurface polarization optics: independent phase control of arbitrary orthogonal states of polarization," Phys. Rev. Lett. **118**, 113901 (2017).

19. B. Yao, X. Zang, Y. Zhu, D. Yu, J. Xie, L. Chen, S. Han, Y. Zhu, and S. Zhuang, "Spin-decoupled metalens with intensity-tunable multiple focal points," Photon. Res. **9**, 1019–1032 (2021).

20. G. Ding, K. Chen, X. Luo, J. Zhao, T. Jiang, and Y. Feng, "Dual-helicity decoupled coding metasurface for independent spin-to-orbital angular momentum conversion," Phys. Rev. Appl. **11**, 044043 (2019).

21. Y. Xu, Q. Li, X. Zhang, M. Wei, Q. Xu, Q. Wang, H. Zhang, W. Zhang, C. Hu, Z. Zhang, C. Zhang, X. Zhang, J. Han, and W. Zhang, "Spin-decoupled multifunctional metasurface for asymmetric polarization generation," ACS Photon. **6**, 2933–2941 (2019).

22. L. Chen, Q. Ma, Q. F. Nie, Q. R. Hong, H. Y. Cui, Y. Ruan, and T. J. Cui, "Dual-polarization programmable metasurface modulator for near-field information encoding and transmission," Photon. Res. **9**, 116–124 (2021).

23. S. J. Li, Y. B. Li, L. Zhang, Z. J. Luo, B. W. Han, R. Q. Li, X. Y. Cao, Q. Cheng, and T. J. Cui, "Programmable controls to scattering properties of a radiation array," Laser Photon. Rev. **15**, 2000449 (2021).

24. W. Tang, J. Y. Dai, M. Chen, X. Li, Q. Cheng, S. Jin, K. Wong, and T. J. Cui, "Programmable metasurface-based RF chain-free 8PSK wireless transmitter," Electron. Lett. **55**, 417–420 (2019).

25. J. Zhao, X. Yang, J. Y. Dai, Q. Cheng, X. Li, N. H. Qi, J. C. Ke, G. D. Bai, S. Liu, S. Jin, A. Alù, and T. J. Cui, "Programmable time-domain digital-coding metasurface for non-linear harmonic manipulation and new wireless communication systems," Natl. Sci. Rev. **6**, 231–238 (2019).

26. W. Tang, M. Z. Chen, X. Chen, J. Y. Dai, Y. Han, M. Di Renzo, Y. Zeng, S. Jin, Q. Cheng, and T. J. Cui, "Wireless communications with reconfigurable intelligent surface: path loss modeling and experimental measurement," IEEE Trans. Wirel. Commun. **20**, 421–439 (2021).

27. P. Ding, Y. Li, L. Shao, X. Tian, J. Wang, and C. Fan, "Graphene aperture-based metalens for dynamic focusing of terahertz waves," Opt. Express **26**, 28038–28050 (2018).

28. J. Huang, B. Hu, K. Muhammad Ismail, W. Liu, and J. Liu, "Graphene-enabled active terahertz focusing with wide tuning range," J. Phys. D **54**, 385104 (2021).

29. W. Liu, B. Hu, Z. Huang, H. Guan, H. Li, X. Wang, Y. Zhang, H. Yin, X. Xiong, J. Liu, and Y. Wang, "Graphene-enabled electrically controlled terahertz meta-lens," Photon. Res. **6**, 703–708 (2018).

30. B. Tang and Y. Ren, "Tunable and switchable multi-functional terahertz metamaterials based on a hybrid vanadium dioxide–graphene integrated configuration," Phys. Chem. Chem. Phys. **24**, 8408–8414 (2022).

31. S. Zhou, Z. Shen, X. Li, S. Ge, Y. Lu, and W. Hu, "Liquid crystal integrated metalens with dynamic focusing property," Opt. Lett. **45**, 4324–4327 (2020).

32. Z. Shen, S. Zhou, X. Li, S. Ge, P. Chen, W. Hu, and Y. Lu, "Liquid crystal integrated metalens with tunable chromatic aberration," Adv. Photon. **2**, 036002 (2020).

33. Z. Shen, S. Zhou, S. Ge, W. Duan, L. Ma, Y. Lu, and W. Hu, "Liquid crystal tunable terahertz lens with spin-selected focusing property," Opt. Express **27**, 8800–8807 (2019).

34. Z. Shen, M. Tang, P. Chen, S. Zhou, S. Ge, W. Duan, T. Wei, X. Liang, W. Hu, and Y. Lu, "Planar terahertz photonics mediated by liquid crystal polymers," Adv. Opt. Mater. **8**, 1902124 (2020).

35. C. Zhang, G. Zhou, J. Wu, Y. Tang, Q. Wen, S. Li, J. Han, B. Jin, J. Chen, and P. Wu, "Active control of terahertz waves using vanadium-dioxide-embedded metamaterials," Phys. Rev. Appl. **11**, 054016 (2019).

36. B. K. Shrewsbury, A. M. Morsy, and M. L. Povinelli, "Multilayer planar structure for optimized passive thermal homeostasis [Invited]," Opt. Mater. Express **12**, 1442–1449 (2022).

37. J.-L. Fang, L. Qu, and H.-L. Yi, "Thermal switching of near-field radiative heat transfer between nanoparticles via multilayered surface modes," Phys. Rev. Appl. **17**, 034040 (2022).

38. K. Nishikawa, M. Yoshimura, and Y. Watanabe, "Growth of nanostructured VO_2 via controlling oxidation of V thin films: morphology and phase transition properties," J. Appl. Phys. **129**, 185303 (2021).

39. K. Nishikawa, M. Yoshimura, and Y. Watanabe, "Phase transition behavior in nanostructured VO_2 with M1, M2, and R phases observed via temperature-dependent XRD measurements," J. Vac. Sci. Technol. A **40**, 033401 (2022).

40. Q. Shi, W. Huang, T. Lu, Y. Zhang, F. Yue, S. Qiao, and Y. Xiao, "Nanostructured VO_2 film with high transparency and enhanced switching ratio in THz range," Appl. Phys. Lett. **104**, 071903 (2014).

41. H. Li, H. Djaoued, J. Robichaud, and Y. Djaoued, "A pleasant blue-green colored 2D vanadium dioxide inverse opal monolayer: large area fabrication and its thermochromic application," J. Mater. Chem. C **8**, 11572–11580 (2020).

42. W. Kou, W. Shi, Y. Zhang, Z. Yang, T. Chen, J. Gu, X. Zhang, Q. Shi, S. Liang, F. Lan, H. Zeng, and Z. Yang, "Terahertz switchable focusing planar lens with a nanoscale vanadium dioxide integrated metasurface," IEEE Trans. Terahertz Sci. Technol. **12**, 13–22 (2021).

43. F. Ding, S. Zhong, and S. I. Bozhevolnyi, "Vanadium dioxide integrated metasurfaces with switchable functionalities at terahertz frequencies," Adv. Opt. Mater. **6**, 1701204 (2018).

44. Y. Ren and B. Tang, "Switchable multi-functional VO_2-integrated metamaterial devices in the terahertz region," J. Lightwave Technol. **39**, 5864–5868 (2021).

45. J. Huang, J. Li, Y. Yang, J. Li, J. Li, Y. Zhang, and J. Yao, "Active controllable dual broadband terahertz absorber based on hybrid metamaterials with vanadium dioxide," Opt. Express **28**, 7018–7027 (2020).

46. M. Mao, Y. Liang, R. Liang, L. Zhao, N. Xu, J. Guo, F. Wang, H. Meng, H. Liu, and Z. Wei, "Dynamically temperature-voltage controlled multifunctional device based on VO_2 and graphene hybrid metamaterials: perfect absorber and highly efficient polarization converter," Nanomaterials **9**, 1101 (2019).

47. H. S. Choi, J. S. Ahn, J. H. Jung, T. W. Noh, and D. H. Kim, "Mid-infrared properties of a VO_2 film near the metal-insulator transition," Phys. Rev. B **54**, 4621–4628 (1996).

48. C. Menzel, C. Helgert, C. Rockstuhl, E.-B. Kley, A. Tünnermann, T. Pertsch, and F. Lederer, "Asymmetric transmission of linearly polarized light at optical metamaterials," Phys. Rev. Lett. **104**, 253902 (2010).

49. T. Wang, H. Zhang, Y. Zhang, Y. Zhang, and M. Cao, "Tunable bifunctional terahertz metamaterial device based on Dirac semimetals and vanadium dioxide," Opt. Express **28**, 17434–17448 (2020).

50. J. Zhao, J. Song, T. Xu, T. Yang, and J. Zhou, "Controllable linear asymmetric transmission and perfect polarization conversion in a terahertz hybrid metal-graphene metasurface," Opt. Express **27**, 9773–9781 (2019).

51. T. J. Cui, M. Q. Qi, X. Wan, J. Zhao, and Q. Cheng, "Coding metamaterials, digital metamaterials and programmable metamaterials," Light Sci. Appl. **3**, e218 (2014).

52. F. Aieta, P. Genevet, M. A. Kats, N. Yu, R. Blanchard, Z. Gaburro, and F. Capasso, "Aberration-free ultrathin flat lenses and axicons at telecom wavelengths based on plasmonic metasurfaces," Nano Lett. **12**, 4932–4936 (2012).

53. V. G. Golubev, V. Yu. Davydov, N. F. Kartenko, D. A. Kurdyukov, A. V. Medvedev, A. B. Pevtsov, A. V. Scherbakov, and E. B. Shadrin, "Phase transition-governed opal-VO_2 photonic crystal," Appl. Phys. Lett. **79**, 2127–2129 (2001).